SLAC-PUB-16909

Uranium(IV) adsorption by natural organic matter in anoxic sediments

Sharon E. Bone[a,1], James J. Dynes[b], John Cliff[c], and John R. Bargar[a]

[a]Stanford Synchrotron Radiation Lightsource, SLAC National Accelerator Laboratory, Menlo Park, CA 94025; [b]Canadian Light Source, Saskatoon, SK S7N 2V3, Canada; and [c]Environmental Molecular Sciences Laboratory, Pacific Northwest National Laboratory, Richland, WA 99354

Edited by Susan L. Brantley, Pennsylvania State University, University Park, PA, and approved November 22, 2016 (received for review July 20, 2016)

Uranium is an important carbon-free fuel source and environmental contaminant that accumulates in the tetravalent state, U(IV), in anoxic sediments, such as ore deposits, marine basins, and contaminated aquifers. However, little is known about the speciation of U(IV) in low-temperature geochemical environments, inhibiting the development of a conceptual model of U behavior. Until recently, U(IV) was assumed to exist predominantly as the sparingly soluble mineral uraninite (UO_{2+x}) in anoxic sediments; however, studies now show that this is not often the case. Yet a model of U(IV) speciation in the absence of mineral formation under field-relevant conditions has not yet been developed. Uranium(IV) speciation controls its reactivity, particularly its susceptibility to oxidative mobilization, impacting its distribution and toxicity. Here we show adsorption to organic carbon and organic carbon-coated clays dominate U(IV) speciation in an organic-rich natural substrate under field-relevant conditions. Whereas previous research assumed that U(IV) speciation is dictated by the mode of reduction (i.e., whether reduction is mediated by microbes or by inorganic reductants), our results demonstrate that mineral formation can be diminished in favor of adsorption, regardless of reduction pathway. Projections of U transport and bioavailability, and thus its threat to human and ecosystem health, must consider U(IV) adsorption to organic matter within the sediment environment.

uranium | organic matter | STXM | NanoSIMS | EXAFS

Uranium serves as an important fuel source and alternative to fossil fuels; however, mining has resulted in widespread contamination (1), which threatens human and ecosystem health. For instance, U is one of the leading pollutants at sites managed by the US Department of Energy (2), with remediation of former mill sites costing the US government $2 billion (as of the year 2000) (3). Uranium accumulates in low-temperature geochemical environments wherever anoxic conditions prevail because U(IV) is much less soluble than U(VI) (tetravalent actinides tend to form stronger complexes with any given ligand than hexavalent actinides and hydrolyze at very low pH values) (4). For many years researchers assumed that sparingly soluble minerals, such as UO_{2+x}, controlled the aqueous concentration of U(IV) and mediated the oxidation of U(IV) to U(VI) under anoxic conditions (5, 6). In fact, many researchers have shown that UO_{2+x} either is not observed in sediments, or is a minor phase (7–13). The chemical reactivity of U(IV) is controlled by its speciation; for instance, researchers have noted that some biogenically produced forms of U(IV), termed "noncrystalline U(IV)," oxidize more rapidly than does UO_{2+x} (14). Thus, knowledge of U(IV) speciation is essential to understand U processes and behavior in low-temperature geochemical environments, including ore deposits (12), marine basins (15, 16), and contaminated aquifers (8). However, an alternative description has not been fully developed to complement U(IV) mineral formation in sediments under environmentally relevant conditions, and this gap represents a major weakness in our geochemical knowledge of this critical element.

Two recent studies have found that U(IV) adsorbs to rutile and magnetite surfaces at low (1 μM) initial aqueous U(IV) concentrations (17, 18). Additionally, researchers have concluded that U(IV) will bind to phosphonate groups associated with bacterial cells and exopolymeric substances (EPS) or form amorphous precipitates with inorganic phosphate in pure cultures of U(VI)-reducing bacteria (19–21). The association of U(IV) with these naturally occurring materials implies that U(IV) could adsorb or become incorporated into sedimentary solids. However, to date, few studies have explicitly examined the role of U(IV) adsorption in sediments under environmental conditions, and no study has identified unambiguously which sorbents bind U(IV). Sediments comprise a mixture of organic and inorganic materials intimately mixed at the nanometer scale. In this complicated matrix it is unknown which materials and types of binding environments will emerge as important for U(IV) sorption. If U(IV) were to adsorb to the sedimentary matrix, we would expect that the formation of U(IV) minerals would be inhibited at low U concentrations, at which binding of U(IV) to surface ligands would suppress the aqueous U^{4+} concentration below the level required for precipitation. No studies examine U(IV) speciation as a function of concentration under field-relevant conditions, which is necessary to understand its complexation behavior.

Our objective was to investigate sorption of U(IV) to a natural sedimentary material as a function of U concentration under field-relevant conditions. Furthermore, we aimed to (*i*) determine whether adsorption complexes could dominate U(IV) speciation at total aqueous U concentrations typical of contaminated aquifers (22), and (*ii*) identify with which sorbents U(IV) was associated (e.g., organic or mineral). Using a combination of extended X-ray absorption fine structure (EXAFS) spectroscopy, scanning transmission X-ray microscopy (STXM), and nanosecondary ion mass spectrometry (NanoSIMS), we present direct evidence that U(IV) adsorbs to particulate organic carbon (POC)

Significance

Uranium is an important fuel source and pollutant, and its chemical form determines its reactivity in the environment. However, information on the speciation of tetravalent U [U(IV)] in sediments is lacking. The research presented herein takes a holistic view of U(IV) speciation in a natural material containing microbial cells, organic matter, and minerals. Our work demonstrates unequivocally that U(IV) adsorbs to natural organic matter under anoxic, field-relevant conditions. Furthermore, we put forward a conceptual model that provides a framework for future studies of U biogeochemistry in which postreduction surface complexation processes can be used to predict U(IV) behavior. Our work has ramifications for remediation of U-contaminated sites and also informs in situ mining practices.

Author contributions: S.E.B. and J.R.B. designed research; S.E.B. performed research; J.J.D., J.C., and J.R.B. contributed new reagents/analytic tools; S.E.B. and J.C. analyzed data; and S.E.B. wrote the paper.

The authors declare no conflict of interest.

This article is a PNAS Direct Submission.

[1]To whom correspondence should be addressed. Email: shbone@slac.stanford.edu.

This article contains supporting information online at www.pnas.org/lookup/suppl/doi:10.1073/pnas.1611918114/-/DCSupplemental.

This material is based upon work supported by the U.S. Department of Energy, Office of Science, under Contract No. DE-AC02-76SF00515.

and organic matter-coated clays in a natural sedimentary material at environmentally relevant U concentrations under sulfate-reducing conditions.

Results

Microcosm Experiments. To determine the role of adsorption in U(IV) speciation and to identify involved sorbents, we prepared batch microcosm experiments in which uranyl acetate (0, 1, 10, 50, and 400 μM) was incubated with macerated roots (from *Phalaris arundinacea*), root-adhering mineral particles, and artificial groundwater under anaerobic (sulfate-reducing) conditions, which drove U(VI) reduction. To assess whether U(IV) could be produced by inorganic reductants generated during anaerobic respiration, we performed complementary batch experiments in which reduction of 10 μM U(VI) was monitored in solutions containing 1 mM aqueous S(−II) (no solids) or suspensions containing 1 mM aqueous S(−II) and autoclaved macerated roots. The microcosms were designed to emulate organic-rich, anoxic, sulfidic sediments identified within the U-contaminated aquifer located in Rifle, CO, which have been proposed to be a source of elevated U concentrations in groundwater (10). Macerated root material was chosen as a substrate because this material (*i*) provided a solid matrix similar to sedimentary material in terms of both elemental composition (9) (*SI Appendix*, Table S1) and organic matter composition (*vide infra*); and (*ii*) was similar to organic material frequently buried in fluvial aquifers, such as the one at Rifle (23). Experimental conditions are summarized in *SI Appendix*, Table S2.

Reduction of U(VI) to U(IV) Under SO_4^{2-}-Reducing Conditions. The native microbial community associated with the root slurry respired sulfate, as indicated by the production of sulfide over the course of the incubation (Fig. 1*A*). Reduced Fe and S species (likely as mackinawite, FeS) were identified in the solid phase during the incubation using S and Fe K-edge XANES spectroscopy, respectively (*SI Appendix*, Figs. S1 and S2 and Table S3). In contrast, reduced species were not formed in sterile controls (*SI Appendix*, Figs. S1 and S2 and Table S3).

A combination of microbial- and surface-catalyzed reduction led to a decrease in aqueous U(VI) and the accumulation of U(IV) in the solid phase. Uranium(VI) reduction was observed in nonsterile samples (Fig. 1*B* and *SI Appendix*, Table S4) and in sterilized root suspensions to which 1 mM aqueous S(−II) had been added (termed "roots + 1 mM $S(-II)_{(aq)}$"; Fig. 1*D*). The production of solid-phase S(−II) and Fe(II) in roots + 1 mM $S(-II)_{(aq)}$ samples (*SI Appendix*, Figs. S1 and S2) suggests that aqueous S(−II) reacted with the root matrix to form solid-phase reductants that catalyzed U(VI) reduction, which has also been observed in Fe(II)-containing systems (24). However, no U(VI) reduction was observed in sterile controls (Fig. 1*C*) or in samples containing only 1 mM S(−II) and artificial groundwater (termed "1 mM $S(-II)_{(aq)}$"; Fig. 1*D*), consistent with the observation that U(VI) reduction by aqueous S(−II) is inhibited by the formation of ternary Ca-U(VI)–CO_3 complexes (25), which dominated under our experimental conditions ($[H_2CO_3] + [HCO_3^-] + [CO_3^{2-}] = 6.8$ mM and $[Ca^{2+}] = 3.5$ mM) (26).

Adsorption of U(IV) to Organic Matter and Clay Particles. Linear combination fits of the EXAFS spectra of $[U(VI)]_{initial}$ = 1, 10, 50, and 400 μM (days 55–69) were performed using spectra from biogenic UO_{2+x} and noncrystalline U(IV) (27). These fits showed UO_{2+x} was only present in suspensions containing >10 μM U (*SI Appendix*, Fig. S3 and Table S5). Additionally, transmission electron microscopy (TEM) images of the 50-μM samples revealed aggregates of 2- to 3-nm UO_{2+x} particles interspersed with amorphous material (assumed to be organic carbon) and other mineral particles (*SI Appendix*, Fig. S4). The dependence of UO_{2+x} formation on the initial U concentration (i.e., U:solid ratio) is consistent with adsorption of U(IV) to the solid matrix, which suppresses $U^{4+}{}_{(aq)}$ concentrations, hence UO_{2+x} precipitation (13). The conclusion that U(IV) adsorption to the sample matrix dominates at 1- and 10-μM U concentrations is supported by our estimation that the concentration of adsorption sites is in great excess of U. For instance, if we use the concentration of carbonyl functional groups present in the organic carbon fraction of humic acids in soils (28) as a proxy for a single type of adsorption site associated with the organic fraction of the sample matrix that may bind U (i.e., carboxylate acids) (4), we find that at carbonyl concentrations ranging from 3 to 25 mol/ kg organic C (28), the molar ratio of adsorption site (i.e., carbonyl) to U ranges between 180 and 1,500 in the 10-μM U sample.

Spatially resolved techniques were used to characterize the sample substrate and to assess the physical associations between U and sample components with nanometer-scale resolution. Images of the 10-μM and 50-μM samples are presented herein (Figs. 2 and 3). Additional images are provided in *SI Appendix* to corroborate the spatial trends and spectroscopic analysis inferred from the images presented in Figs. 2 and 3. Microscopy images revealed that the samples consisted of aggregates of organic carbon particles, defined here as POC, and minerals, including aluminosilicates. The latter were identified based on the correlation between Fe and Al (29) in NanoSIMS images (R^2_{Al-Fe} = 0.61–0.81; Fig. 2 and *SI Appendix*, Fig. S6 and Tables S6 and S7), as well as the cooccurrence of Fe, Al, and Si in the STXM images (*SI Appendix*, Fig. S7). The characterization of the POC is discussed in detail in *SI Appendix*, section VI. Briefly, POC consisted of identifiable plant material (including lignin and polysaccharides), microbial cells, and partially degraded organic matter that was not attributable to any one biomolecule.

Spatial correlation analysis of the 10-μM U sample revealed that adsorbed U was correlated with C (R^2 = 0.51–0.67) and was enriched in some areas of the 10-μM sample where whole, intact microbial cells were identified based on morphology (Fig. 2). Uranium was also correlated with S (R^2 = 0.57–0.82; Fig. 2 and

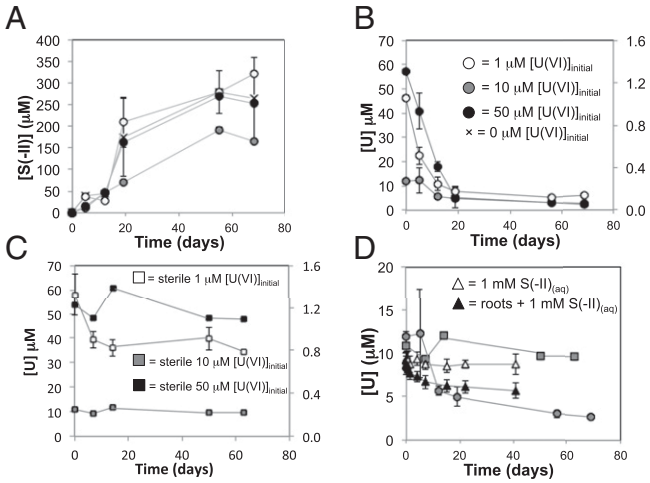

Fig. 1. Production of $S(-II)_{(aq)}$ and attenuation of $U_{(aq)}$ in incubated samples. The aqueous S(−II) concentration in nonsterile incubations is plotted in *A*. The aqueous U concentration in nonsterile incubations is plotted in *B* and in sterile controls in *C*. The aqueous U concentration in samples containing $[U(VI)]_{initial}$ = 1 μM is always plotted on the right-hand *y* axis. Error bars denote one SD for four replicate samples (first two time-points), triplicate samples (second two time-points), or duplicate (penultimate time-point). The concentration of aqueous U in the roots + 1 mM S(−II) and 1-mM $S(-II)_{(aq)}$ samples are shown in *D*. Error bars denote one SD from three replicate samples. The sterile and nonsterile incubation 10-μM U samples are replotted in *D* for comparison.

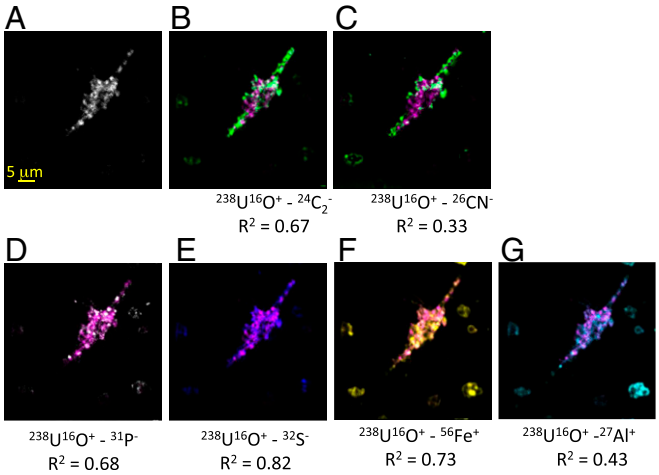

Fig. 2. NanoSIMS images of U, C, N, Fe, Al, S, and P distribution in the nonsterile $[U(VI)]_{initial}$ = 10 µM, 68-d sample. Images show the location of U, which is shown in gray in *A* and in pink in *B*–*G*. The locations of C, N (as CN^-), P, S, Fe, and Al are shown in *B*, *C*, *D*, *E*, *F*, and *G*, respectively. The spherical and rod-shaped objects observed in *B* and *C* are interpreted to be bacterial cells. The pixel size is 200 nm. The Pearson correlation coefficient (R^2) between the $^{238}U^{16}O^+$ ion and each ion is given below the corresponding image. The scale bar is the same for all images.

SI Appendix, Fig. S6 and Tables S6 and S7), which was, in turn, highly correlated with C (R^2 = 0.80–0.87). Sulfur was present dominantly in thiol and inorganic sulfide groups, based on the bulk S K-edge spectra. Because U does not readily form bonds with reduced S species (4), which are soft bases, the U–S correlation could have arisen if thiol-S was associated with organic matter types that had a high affinity for U.

We had expected that U would be spatially associated with P due to complexation between U and inorganic or organic P ligands (19). However, U and P were not always well correlated in the 10-µM sample (R^2 = 0.19–0.68; Fig. 2 and *SI Appendix*, Fig. S6 and Tables S6 and S7), and P was found to be concentrated in hot spots, whereas U was more diffusely distributed. Because P was not highly correlated with C (for the 10-µM sample, R^2 = 0.25–0.47; *SI Appendix*, Tables S6 and S7), it is unlikely we detected organic P. Thus, the absence of a correlation between P and U does not preclude the complexation of U by organic P. However, it does appear that inorganic P was not important for U complexation in our samples, which further suggests that amorphous U–PO_4 precipitates (21) are a minor species or are absent in these samples.

Uranium was associated with C in the 50- and 400-µM samples. Regions in these samples were examined using both STXM and NanoSIMS, allowing direct insight into the C speciation in areas enriched in U. Fig. 3 presents complementary STXM and NanoSIMS images of the 50-µM sample; furthermore, specific regions within Fig. 3 (labeled R1–R5) are discussed below, and their elemental compositions and functional group character are summarized in Table 1. The images showed that U was frequently associated with cells [based on their morphology and the presence of protein-like spectra (30); Fig. 3, region 1 Table 1, and *SI Appendix*, Figs. S7, S11, and S12], as expected, because research has shown that bacterial cells and EPS reduce U(VI) and readily complex U(IV) (19, 20). Uranium was also associated with partially degraded organic material (29) and possibly EPS (31) (*SI Appendix*, Figs. S7, S11, and S12), which contained carboxylate functional groups that could have complexed U.

Uranium-enriched areas were identified that contained plant-derived materials, deduced from their similarity to lignin (Fig. 3, region 3 and Table 1), the presence of a peak in the O-alkyl C region [indicative of polysaccharides (32); Fig. 3, region 4 and Table 1] and the presence of quinones (33, 34) (Fig. 3, region 4 and Table 1). Plant material has not been shown to adsorb U(IV) previously; however, it is possible that phenols and carboxylate groups could complex U(IV) (4). Additionally, UO_{2+x} nanoparticles, which were detected at 50 µM U, could have aggregated with the plant material subsequent to their formation. Finally, U could have been associated with Fe-, Al-, and S-containing particles, because these elements were enriched in regions 3 and 4 (Fig. 3 and Table 1). Indeed, region 5 (Fig. 3 and Table 1), which was not enriched in U, was composed of plant-derived material (Table 1), but exhibited little S, Fe, and Al relative to other particles, emphasizing a possible role for these elements in controlling the distribution of U.

In addition to the association of U(IV) with POC, we found U to be associated with aluminosilicate particles. For the 10-µM sample, $R^2_{U–Fe}$ = 0.59–0.73 and $R^2_{U–Al}$ = 0.43–0.60 (Fig. 2 and *SI Appendix*, Fig. S6 and Tables S6 and S7) and for the 50-µM sample, $R^2_{U–Fe}$ = 0.84 and $R^2_{U–Al}$ = 0.75 (Fig. 3). Uranium was typically associated with clay particles that were coated with organic material. Indeed, one clay particle was imaged that was not coated in C; in this instance, U was not associated with the particle (*SI Appendix*, Fig. S6), leading us to speculate that U(IV) was adsorbed to organic matter sorbed to the clays. Because Fe(II) in clays can reduce U(VI) (35), it is possible that the correlation among U, Fe, and Al could have arisen in part due to reduction of U(VI) by the clay particles. Iron was also correlated

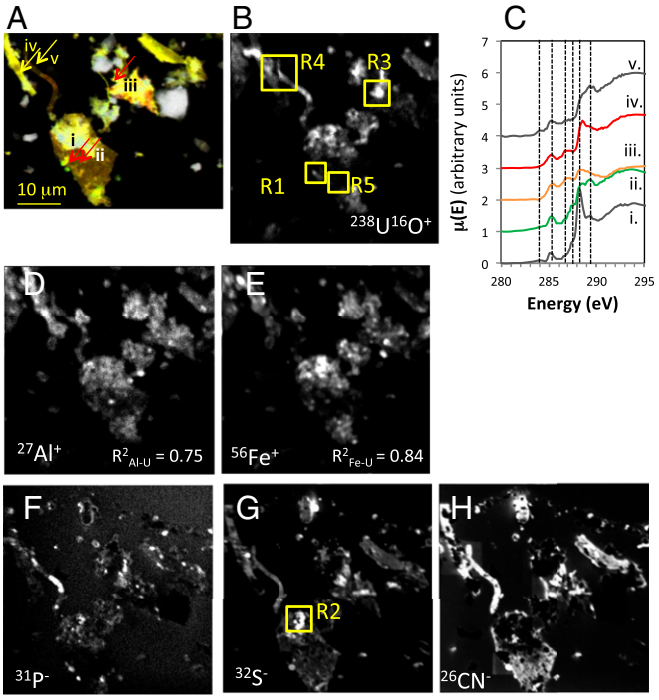

Fig. 3. Distribution of U, C, Al, Fe, P, S, and N in nonsterile $[U(VI)]_{initial}$ = 50 µM, 68 d. The organic carbon distribution determined via STXM (spatial resolution = 150 nm) (*A*) is compared with the U, Al, Fe, P, S, and N (as CN^-) distributions determined via NanoSIMS (pixel size = 200 nm) (*B* and *D*–*H*). (*A*) Image difference map showing 288.2 eV (green) and 289.5 eV (red) relative to 280 eV (gray). The yellow regions indicate the areas where red and green overlap. Carbon K-edge stack maps were collected for select, smaller regions within *A*, and spectra, labeled *i*–*v* from these regions are plotted in *C*. The dotted lines in *C* highlight the dominant peaks found in the various spectra (Table 1). Yellow boxes denote regions (R1–R5) that are discussed in the text; key features are summarized in Table 1. The scale bar is the same for all images.

Table 1. Spectroscopic analysis and elemental composition of regions highlighted in Fig. 3

Region	Spectrum	Elements enriched	Energies of major peaks, eV	Carbon functional groups (ref.)	Compound class	Origin
1	(i)	U, C, S, N, P	285.4, 288.2, 289.4	Aromatic (34), carboxylate/amide (52), O-alkyl (34)	Protein	Microbial
2	NA	U, C, S, Fe, Al, P	NA	NA	NA	NA
3	(iii)	U, C, S, Fe, Al, N, P	285.5, 287.0, 288.4	Aromatic, phenolic (34), carboxylate	Lignin	Plant
4	(iv)	U, C, S, Fe, Al	285.4, 286.7, 288.5, 289.3	Aromatic, ketone (34), carboxylate, O-alkyl	Mixed	Partially degraded material/plant
4	(v)	U, C, S, N, P	284.0, 285.3, 287, 288.7, 289.3	Quinone (34), aromatic, phenolic, carboxylate, O-alkyl	Mixed, quinones, polysaccharide	Plant
5	(ii)	C	285.4, 287.3, 288.5, 289.3	Aromatic, phenolic, carboxylate, O-alkyl	Mixed, polysaccharide	Plant

See *SI Appendix*, section VI for details of energy assignments, compound classes, and compound class origin. NA, not applicable.

with S in the images (particularly in Fig. 2; $R^2 = 0.73$), and particles that were enriched in U, Fe, and S were identified (Fig. 3, region 2 and *SI Appendix*, Fig. S6), consistent with U(VI) reduction by FeS.

Analysis of the molecular-scale coordination environment of U using shell-by-shell EXAFS spectroscopic analysis supported the interpretation that U(IV) was adsorbed to organic matter. Based on our observation that U was associated with POC and organic carbon-coated minerals, in combination with knowledge of the functional groups that bind U strongly (phosphate esters and carboxylates) (4, 19), we fit the EXAFS spectra assuming that U was coordinated to either C or P in its second shell, which yielded a good representation of the data (Fig. 4 and *SI Appendix*, Table S11 present the fits with the U-C scattering path, and *SI Appendix*, Fig. S14 and Table S12 present the fits with the U-P scattering path). Our spectroscopic analysis could not yield information on the coordination of U to clay minerals, because high-atomic number neighbors were not evident (see *SI Appendix* for details).

Discussion

Mixed Biotic–Abiotic U(VI) Reduction Pathways in Sediments. Under acetate-stimulated sulfate-reducing conditions in Rifle aquifer sediments, Bargar et al. (8) observed that U(IV) was physically associated with FeS particles at micron- to millimeter-length scales, but U and FeS were not correlated at the nanometer scale. The authors thus proposed a biotic–abiotic reduction pathway in which FeS particles served as a reservoir of electrons for U(VI) reduction, and that reduction was mediated by biomass-associated ligands as well as microbial reductases. Similarly, we infer that coupled biotic–abiotic U(VI) reduction occurs in SO_4^{2-}-reducing sediments based on our observations that (*i*) U(VI) was reduced most rapidly in the presence of actively respiring microbes; (*ii*) U(VI) reduction occurred in the absence of actively respiring microbes when solid-phase S(−II) and Fe(II) accumulated; and, finally, (*iii*) U was sometimes physically associated with solid-phase inorganic reductants, including Fe and S. We propose that aggregates of cells, organic matter, FeS, and aluminosilicates serve as micrometer-scale "reduction hotspots" where numerous U(VI) reductants cooccur, facilitating the transformation of U(VI) to U(IV). Uranium(IV) subsequently adsorbs to high-affinity ligands associated with the aggregates.

Evidence for U(IV) Adsorption Complexes: Implications for U(IV) Biogeochemistry. Using spectroscopy and nanoscale microscopy, we have provided direct evidence that U(IV) adsorbs to organic matter and organic matter-coated clay particles in a complex natural matrix comprising a mixture of organic and mineral phases. Few researchers have investigated the adsorption behavior of U(IV) as a function of U concentration because UO_{2+x} is highly insoluble, making it difficult to apply traditional measurements (e.g., adsorption isotherms) (36). However, Latta et al. (18) found that U(IV) adsorbed to magnetite and rutile at surface loadings less than ∼4,000 ppm; whereas UO_{2+x} precipitated at surface loadings of 24,000 ppm (magnetite) and 12,000 ppm (rutile). The root solid used in this research had a lower affinity for U(IV), because inhibition of UO_{2+x} occurred in samples containing <2,500 ppm U. However, our model system provides a closer representation of sediments than do pure mineral phases, which suggests that UO_{2+x} formation will be inhibited in many subsurface environments as the result of binding to organic matter and organic matter–mineral aggregates.

Researchers have suggested that different mechanisms of U(VI) reduction [e.g., by sulfate-reducing bacteria or their inorganic products (FeS) (8) or by Gram-positive or -negative bacteria (37)] yield different U(IV) products, i.e., that the reduction pathway dictates the products. For example, the formation of similar U(IV) species in sediments during a redox transition was used to infer that the same U(VI) reduction mechanism was operating under both Fe- and SO_4^{2-}-reducing conditions (7). However, our observation that we can induce the formation of adsorbed U(IV) relative to UO_{2+x} simply by changing the ratio of U to solid concentration in our sample suspensions implies that the number of sites available to bind U(IV) can exert control over UO_{2+x} formation, regardless of the reduction pathway.

The utility of a model in which U(IV) can adsorb to the sedimentary matrix subsequent to reduction is that it reconciles

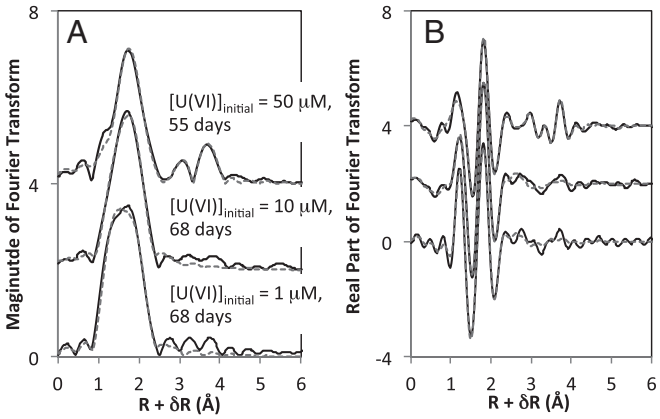

Fig. 4. Fourier-transformed EXAFS spectra of nonsterile $[U(VI)]_{initial}$ = 1 and 10 μM, day-68 samples, and $[U(VI)]_{initial}$ = 50 μM, day-55 samples. The magnitude (*A*) and real part (*B*) of the Fourier-transformed EXAFS spectra for 1-, 10-, and 50-μM U samples are shown. The experimental spectra are shown in black, and the fits are shown in gray.

disparate published observations that noncrystalline U(IV) is favored (*i*) in the presence of elevated orthophosphate (19, 21, 37–39), which is expected to have a very high affinity for U(IV) (4); (*ii*) upon enhancement of EPS formation in pure cultures (40), which increases the number of high-affinity U(IV) ligands; and (*iii*) in both nonsterile and sterile biofilms, in which U(VI) is reduced via a direct or indirect pathway, respectively (40). Our research further implies that models that seek to predict U behavior in the subsurface, e.g., for the purpose of remediation of contaminated groundwater (41) or in situ mining of U roll-front ore deposits (12), should include U(IV) complexation reactions, especially with organic matter. Research is needed to quantify the affinity of U(IV) for whole sediments and individual environmentally important solid phases, as has been done for U(VI). In particular, the affinity of specific organic moieties for U(IV), and the potential for U(IV) to form complexes with organic coatings on minerals or ternary organic mineral complexes, should be investigated. Finally, adsorbed U(IV) is likely to be more kinetically labile than UO_{2+x} (14, 27), and this has important ramifications for U mobility in the environment: U(IV) could be more mobile under anoxic conditions than anticipated, and more sensitive to redox fluctuations, with implications for the longevity of U contamination in the subsurface (10) as well as its extractability from ores (12).

Methods

Batch Reactor Design. Root material, collected along the Roaring Fork riverbank in Basalt, CO (proximal to Rifle, CO), was chosen as an analog for root biomass present in Rifle-reduced sediments (10, 23) and was stored in a refrigerator in canning jars until processed. The root material was first rinsed in Milli-Q water (18.2 MΩ·cm) at least three times to remove excess sand and sediment, and then macerated by blending with Milli-Q water to create a slurry. An aliquot of this slurry was dispensed into serum vials, which were then filled with 100 mL artificial groundwater, sealed with 1-cm-thick butyl rubber stoppers and crimp tops, and sparged with 2.5% CO_2/97.5% (vol/vol) N_2 gas for 3 h. The artificial groundwater contained 7 mM SO_4^{2-}, 6.8 mM inorganic carbon (IC = H_2CO_3, HCO_3^-, and CO_3^{2-}), 3.5 mM Ca^{2+}, 3.5 mM Mg^{2+}, 86 μM PO_4^{3-}, and 64 μM NO_3^-. A subset of the samples was autoclaved after sparging to serve as abiotic controls. The final concentration of the solid phase (i.e., root material) in the samples in units of dry mass per volume solution was calculated to be 6 g/L by drying known masses of root slurry in an oven (105 °C, 24 h). The elemental composition of the dried root slurry was measured on an X-ray fluorescence analyzer (AMETEK Material Analysis Division, Spectro XEPOS; metals, S and P content) and an elemental analyzer (Carlo Erba NA1500; C and N content).

Uranyl acetate stock solution was added to the sparged samples using sterile syringes and needles inside a Coy anaerobic chamber with a H_2/N_2 atmosphere [∼2–3% (vol/vol) H_2]. The initial U(VI) concentration was 0, 1, 10, or 50 μM. The pH of the solution was adjusted to ∼7.0 by adding a small volume (<1 mL) of 0.1 M sodium hydroxide. One milliliter of groundwater from well MNA-01 (Rifle, CO) was added to the nonsterile samples to inoculate the samples with the groundwater microbial community from that site. Finally, sealed serum vials were placed on a shaker (outside of the anaerobic chamber) for ∼70 d. Briefly, 4 mL of solution were removed approximately every 10 d using a syringe inside the anaerobic chamber for measurement of total aqueous U and sulfide. Each sample condition was made in quadruplicate. One of the four bottles was killed for analysis of the solid phase after 5, 19, 55, and 68 d. Only for the last time point was there a single sample (no replicates). The solid phase was preserved by storing in an anaerobic canister at −20 °C.

A second set of experiments was performed to test whether inorganic reductants (e.g., HS^-, FeS) generated during the anaerobic incubations of the root material could have reduced U(VI) in the nonsterile root suspensions. Samples were prepared as described above with an initial U(VI) concentration of 10 μM; however, no root slurry was added. Instead, 1 mM $Na_2S_{(aq)}$ was added to serve as the U(VI) reductant [referred to as $S(-II)_{(aq)}$-only samples]. The S(−II) concentration was chosen to exceed the amount generated in the anaerobic incubations to ensure that the rate of U(VI) reduction was not limited by the S(−II) concentration. Additionally, U(VI) reduction was monitored in triplicate sterile root suspensions to which 1 mM $S(-II)_{(aq)}$ was added to assess whether solid-phase reductants generated by the reaction of $S(-II)_{(aq)}$ with the sterile roots could reduce U(VI) [referred to as root + $S(-II)_{(aq)}$ samples]. Uranyl was allowed to equilibrate with the sterilized root suspension for 1 d before addition of $Na_2S_{(aq)}$, after which the pH was adjusted to 7.0. Samples were placed on the shaker for 41 d. As before, aliquots were removed (and filtered through 0.22-μm filters) for analysis of aqueous U and S(−II).

A third set of experiments was performed to generate samples with concentrations of U(IV) great enough to be detectable using STXM. Suspensions of the root material were made in triplicate, as described above, and allowed to incubate for 69 d. Uranyl acetate stock solution was added to the serum bottles in the anaerobic chamber using a syringe every 2 wk to achieve a final concentration of 400 μM U without precipitating U(VI) minerals. A small volume of sample was removed before and after addition of new uranyl acetate stock and filtered for measurement of aqueous U.

Analysis of Aqueous Phase. Aqueous, filtered samples were preserved for analysis of U via inductively coupled plasma-mass spectrometry (ICP-MS; Thermo XSeries II) by acidifying [to 2% (vol/vol) HNO_3]. A second aliquot (1 mL) was preserved for sulfide measurement using 100 μL of 0.1 M zinc acetate. Sulfide was measured using the methylene blue colorimetric technique. Briefly, 60 μL each of 0.085 M *N*,*N*-dimethyl-1,4-phenylenediamine sulfate in 6 M HCl and 0.04 M ferric chloride in 6 M HCl were added to the preserved sample and allowed to react for at least 1 h before measurement at 600 nm using a UV-visible spectrometer (Shimadzu UV-1601).

Scanning Transmission X-ray Microscopic Analysis. STXM was performed at the SM (10ID-1) beamline at the Canadian Light Source (CLS). Two microliters of the root suspension were drop-deposited onto 100-nm-thick silicon nitride windows and fastened onto an Al sample plate in the anaerobic chamber. These samples were transferred in air into the sample chamber at the beamline, which was then evacuated and refilled with He gas to 0.2 atm.

Images were collected in transmission and then converted to optical density by normalization to the incident flux (I_0), as measured in each image in a part of the sample without any particles. All STXM data processing and analysis was performed using aXis2000. Image difference maps were collected at the C, Al, and Si K edges, the Fe $L_{II,III}$ edge, and the U N_{d5} edge by subtracting an OD image of an energy below the edge from an OD image of an energy above the edge. Specifically, optical density images collected at 288.2, 289.5, and 290.6 eV were selected to target 1s → π* resonances characteristic of proteins, polysaccharides, and carbonates, respectively (34). Optical density images collected at 708 and 710 eV were selected to target Fe(II) and Fe(III), respectively (42). Stack maps, in which X-ray absorption spectra were obtained for each pixel within the entire region, were measured at the C and U edges. Energy calibration of the sample spectra was performed using potassium (297.23 and 299.92 eV) (43). Significant beam damage is not expected under the experimental conditions (44). Carbon stack maps were analyzed using principal component and cluster analysis (45), and peak resonances in the C XAS were identified through comparison with literature-reported values for various compounds (full discussion provided in *SI Appendix*, section VI).

NanoSIMS Analysis. NanoSIMS images for the ions were collected at the Environmental Molecular Sciences Laboratory (EMSL) at the Pacific Northwest National Laboratory (PNNL) using a Cameca NanoSIMS 50L. Samples were coated with 10 nm of high purity gold to improve conductivity. Analysis areas were presputtered with 10^{16} ions·cm^{-2}. Images of $^{238}U^{16}O^+$, $^{56}Fe^+$, and $^{27}Al^+$, were acquired in multicollection mode using a ∼15 pA O^- primary beam that had a diameter of ∼300 nm. Special care was made to resolve $^{56}Fe^+$ from $^{28}Si_2^+$ and $^{40}Ca^{16}O^+$. Mass calibration for $^{238}U^{16}O^+$ was achieved using a dried droplet of an ICP-MS U standard. We tested whether the U signal was artifactually caused by isobaric interferences by measuring U in replicate samples prepared without added U, which demonstrated that U was not detected when it was not present (*SI Appendix*, Fig. S5). Ion images of $^{24}C^{2-}$, $^{26}CN^-$, $^{31}P^-$, and $^{32}S^-$ were acquired using a ∼2pA Cs^+ primary beam with a diameter of ∼100 nm. Special care was used to resolve $^{31}P^-$ from $^{30}Si^1H^-$. Images in both polarities were acquired at 256 × 256 pixel resolution with a dwell time of 27 ms·pixel^{-1} for positive ions and 13.5 ms·pixel^{-1} for negative ions.

Analysis of the images was performed using OpenMIMS and ImageJ (46). Dead-time–corrected images were aligned using the ImageJ plug-ins Stackreg and Turboreg so that it was possible to determine how well the different ion intensities correlated on a pixel-by-pixel basis (based on the Pearson correlation coefficient, performed using a correlation indices plugin for ImageJ). Although the beam diameter was different between polarities, the pixel size of each image was the same, 200 nm, thus allowing the intensities of each pixel to be compared between aligned positive and negative ion images. It was possible to align all ion maps for the sample $[U(VI)]_{initial}$ = 10 μM, 68 d. However, the negative ions were offset from the positive ions

by too large a distance for alignment in the samples $[U(VI)]_{initial}$ = 50 μM, 68 d and $[U(VI)]_{initial}$ = 400 μM.

Bulk X-ray Absorption Analysis. Uranium L_{III}-edge X-ray absorption spectra were collected at beamline 11-2 at the Stanford Synchrotron Radiation Lightsource (SSRL). The energy of the X-ray beam was selected using a Si (220) $\varphi = 0$ double-crystal monochromator detuned by 30% at 17,700 eV to minimize harmonics. Calibration was monitored during each sample scan by collecting the Y K edge (17,038.4 eV). The fluorescence signal was monitored using a 100-element Ge detector. A strontium foil and Soller slits were used to increase the signal-to-noise ratio. Beam damage was not observed during measurement of sequential scans, as expected (47).

Background subtraction and linear combination fitting of the spectra to obtain the U oxidation state were performed using the Athena module of the IFFEFIT package (48). The EXAFS spectra were extracted from the normalized absorption spectra by fitting a spline to the region between approximately k = 1 and 10 $Å^{-1}$. The U L_{III}-edge EXAFS spectra were examined using a combination of PCA, target transform analysis, linear combination fitting, and shell-by-shell fitting [using the IFFEFIT package (48)]. The theoretical scattering paths that were used to produce the models of the FT-EXAFS spectra were calculated in FEFF 6L using atomic coordinates derived for UO_{2+x} (49), rutherfordine (50), and ninyoite (51). Details of the fitting procedure are provided in *SI Appendix*, section VII.

ACKNOWLEDGMENTS. The authors thank Ann Marshall for assistance in collecting TEM images at the Stanford Nano Shared Facilities. Funding was provided by the DOE Office of Biological and Environmental Research (BER), Subsurface Biogeochemistry Research activity to the SLAC Science Focus Area program under contract DE-AC02-76SF00515 to SLAC (S.E.B. and J.R.B.). Use of the Stanford Synchrotron Radiation Lightsource (SSRL) is supported by the US DOE, Office of Basic Energy Sciences. A portion of the research was performed using the Environmental Molecular Sciences Laboratory, a DOE Office of Science User Facility sponsored by the Office of BER (located at Pacific Northwest National Laboratory). Research described in this paper was performed at beamline 10ID-1 at the Canadian Light Source (CLS), which is supported by Natural Sciences and Engineering Research Council, Canadian Institutes of Health Research, National Research Council, Western Economic Diversification Canada, the University of Saskatchewan, and the Province of Saskatchewan.

1. Campbell KM, Gallegos TJ, Landa ER (2015) Biogeochemical aspects of uranium mineralization, mining, milling, and remediation. *Appl Geochem* 57:206–235.
2. Hazen T, Faybishenko B, Jordan P (2008) *Complexity of Groundwater Contaminants at DOE Sites* (Lawrence Berkeley National Laboratory, Berkeley).
3. Robinson P (2004) *Uranium Mill Tailings Remediation Performed by the US DOE: An Overview* (Southwest Research and Information Center, Albuquerque, NM). Available at https://www.vbgov.com/government/departments/public-utilities/Documents/08.DOE_Overview_Uranium_Tailing_Remediation.pdf.
4. Choppin G, Jensen M (2006) Actinides in solution: Complexation and kinetics. *The Chemistry of the Actinide and Transactinide Elements*, eds Morss L, Edelstein N, Fuger J (Springer, Dordrecht, The Netherlands), pp 2524–2621.
5. Yabusaki SB, et al. (2007) Uranium removal from groundwater via in situ biostimulation: Field-scale modeling of transport and biological processes. *J Contam Hydrol* 93(1-4):216–235.
6. Schofield EJ, et al. (2008) Structure of biogenic uraninite produced by *Shewanella oneidensis* strain MR-1. *Environ Sci Technol* 42(21):7898–7904.
7. Alessi DS, et al. (2014) Speciation and reactivity of uranium products formed during in situ bioremediation in a shallow alluvial aquifer. *Environ Sci Technol* 48(21): 12842–12850.
8. Bargar JR, et al. (2013) Uranium redox transition pathways in acetate-amended sediments. *Proc Natl Acad Sci USA* 110(12):4506–4511.
9. Campbell KM, et al. (2012) Geochemical, mineralogical and microbiological characteristics of sediment from a naturally reduced zone in a uranium-contaminated aquifer. *Appl Geochem* 27(8):1499–1511.
10. Janot N, et al. (2016) Physico-chemical heterogeneity of organic-rich sediments in the Rifle Aquifer, CO: Impact on uranium biogeochemistry. *Environ Sci Technol* 50(1):46–53.
11. Sharp JO, et al. (2011) Uranium speciation and stability after reductive immobilization in aquifer sediments. *Geochim Cosmochim Acta* 75(21):6497–6510.
12. WoldeGabriel G, et al. (2014) Characterization of cores from an in-situ recovery mined uranium deposit in Wyoming: Implications for post-mining restoration. *Chem Geol* 390:32–45.
13. Mikutta C, Langner P, Bargar JR, Kretzschmar R (2016) Tetra- and hexavalent uranium forms bidentate-mononuclear complexes with particulate organic matter in a naturally uranium-enriched peatland. *Environ Sci Technol* 50(19):10465–10475.
14. Cerrato JM, et al. (2013) Relative reactivity of biogenic and chemogenic uraninite and biogenic noncrystalline U(IV). *Environ Sci Technol* 47(17):9756–9763.
15. Brennecka GA, Herrmann AD, Algeo TJ, Anbar AD (2011) Rapid expansion of oceanic anoxia immediately before the end-Permian mass extinction. *Proc Natl Acad Sci USA* 108(43):17631–17634.
16. Wang X, Johnson TM, Lundstrom CC (2015) Isotope fractionation during oxidation of tetravalent uranium by dissolved oxygen. *Geochim Cosmochim Acta* 150:160–170.
17. Wang ZM, Ulrich KU, Pan C, Giammar DE (2015) Measurement and modeling of U(IV) adsorption to metal oxide minerals. *Environ Sci Technol Lett* 2(8):227–232.
18. Latta DE, Mishra B, Cook RE, Kemner KM, Boyanov MI (2014) Stable U(IV) complexes form at high-affinity mineral surface sites. *Environ Sci Technol* 48(3):1683–1691.
19. Alessi DS, et al. (2014) The product of microbial uranium reduction includes multiple species with U(IV)-phosphate coordination. *Geochim Cosmochim Acta* 131:115–127.
20. Stylo M, et al. (2013) Biogeochemical controls on the product of microbial U(VI) reduction. *Environ Sci Technol* 47(21):12351–12358.
21. Bernier-Latmani R, et al. (2010) Non-uraninite products of microbial U(VI) reduction. *Environ Sci Technol* 44(24):9456–9462.
22. Williams KH, et al. (2011) Acetate availability and its influence on sustainable bioremediation of uranium-contaminated groundwater. *Geomicrobiol J* 28(5-6):519–539.
23. Arora B, et al. (2016) Influence of hydrological, biogeochemical and temperature transients on subsurface carbon fluxes in a flood plain environment. *Biogeochemistry* 127(2-3):367–396.
24. Behrends T, Van Cappellen P (2005) Competition between enzymatic and abiotic reduction of uranium(VI) under iron reducing conditions. *Chem Geol* 220:315–327.
25. Hyun SP, Davis JA, Hayes KF (2014) Abiotic U(VI) reduction by aqueous sulfide. *Appl Geochem* 50:7–15.
26. Dong W, Brooks SC (2006) Determination of the formation constants of ternary complexes of uranyl and carbonate with alkaline earth metals (Mg2+, Ca2+, Sr2+, and Ba2+) using anion exchange method. *Environ Sci Technol* 40(15):4689–4695.
27. Alessi DS, et al. (2012) Quantitative separation of monomeric U(IV) from UO2 in products of U(VI) reduction. *Environ Sci Technol* 46(11):6150–6157.
28. Essington ME (2004) Organic matter in soil. *Soil and Water Chemistry: An Integrative Approach* (CRC, Boca Raton, FL).
29. Wan J, Tyliszczak T, Tokunaga TK (2007) Organic carbon distribution, speciation, and elemental correlations within soil microaggregates: Applications of STXM and NEXAFS spectroscopy. *Geochim Cosmochim Acta* 71(22):5439–5449.
30. Keiluweit M, et al. (2012) Nano-scale investigation of the association of microbial nitrogen residues with iron (hydr)oxides in a forest soil O-horizon. *Geochim Cosmochim Acta* 95(0):213–226.
31. Liu X, et al. (2013) STXM and NanoSIMS investigations on EPS fractions before and after adsorption to goethite. *Environ Sci Technol* 47(7):3158–3166.
32. Boyce CK, et al. (2002) Organic chemical differentiation within fossil plant cell walls detected with X-ray spectromicroscopy. *Geology* 30(11):1039–1042.
33. Kinyagi J, et al. (2006) Nanoscale biogeocomplexity of the organomineral assemblage in soil: Application of STXM microscopy and C 1s-NEXAFS spectroscopy. *Soil Sci Soc Am J* 70(5):1708–1718.
34. Solomon D, et al. (2009) Carbon (1s) NEXAFS spectroscopy of biogeochemically relevant reference organic compounds. *Soil Sci Soc Am J* 73(6):1817–1830.
35. Luan F, Gorski CA, Burgos WD (2014) Thermodynamic controls on the microbial reduction of iron-bearing nontronite and uranium. *Environ Sci Technol* 48(5):2750–2758.
36. Wang Z, et al. (2013) Adsorption of uranium(VI) to manganese oxides: X-ray absorption spectroscopy and surface complexation modeling. *Environ Sci Technol* 47(2):850–858.
37. Boyanov MI, et al. (2011) Solution and microbial controls on the formation of reduced U(IV) species. *Environ Sci Technol* 45(19):8336–8344.
38. Rui X, et al. (2013) Bioreduction of hydrogen uranyl phosphate: Mechanisms and U(IV) products. *Environ Sci Technol* 47(11):5668–5678.
39. Veeramani H, et al. (2011) Products of abiotic U(VI) reduction by biogenic magnetite and vivianite. *Geochim Cosmochim Acta* 75(9):2512–2528.
40. Stylo M, Neubert N, Roebbert Y, Weyer S, Bernier-Latmani R (2015) Mechanism of uranium reduction and immobilization in *Desulfovibrio vulgaris* biofilms. *Environ Sci Technol* 49(17):10553–10561.
41. Yabusaki SB, et al. (2011) Variably saturated flow and multicomponent biogeochemical reactive transport modeling of a uranium bioremediation field experiment. *J Contam Hydrol* 126(3-4):271–290.
42. Dynes JJ, Regier TZ, Snape I, Siciliano SD, Peak D (2015) Validating the scalability of soft X-ray spectromicroscopy for quantitative soil ecology and biogeochemistry research. *Environ Sci Technol* 49(2):1035–1042.
43. Moffet RC, et al. (2010) Microscopic characterization of carbonaceous aerosol particle aging in the outflow from Mexico City. *Atmos Chem Phys* 10(3):961–976.
44. Dynes JJ, et al. (2006) Quantitative mapping of chlorhexidine in natural river biofilms. *Sci Total Environ* 369(1-3):369–383.
45. Lerotic M, Jacobsen C, Schäfer T, Vogt S (2004) Cluster analysis of soft X-ray spectromicroscopy data. *Ultramicroscopy* 100(1-2):35–57.
46. Abramoff MD, Magalhaes PJ, Ram SJ (2004) Image processing with ImageJ. *Biophotonics International* 11(7):36–42.
47. Alessi DS, Uster B, Borca CN, Grolimund D, Bernier-Latmani R (2013) Beam-induced oxidation of monomeric U(IV) species. *J Synchrotron Radiat* 20(Pt 1):197–199.
48. Ravel B, Newville M (2005) ATHENA, ARTEMIS, HEPHAESTUS: Data analysis for X-ray absorption spectroscopy using IFEFFIT. *J Synchrotron Radiat* 12(Pt 4):537–541.
49. Wyckoff RWG (1963) *Crystal Structures 1* (Interscience, New York), 2nd Ed.
50. Finch R, Cooper MA, Hawthorne FC, Ewing RC (1999) Refinement of the crystal structure of rutherfordine. *Can Mineral* 37:929–938.
51. Anthony JW, Bideaux RA, Bladh KW, Nichols MC *Handbook of Mineralogy* (Mineralogical Society of America, Chantilly, VA).
52. Haberstroh PR, et al. (2006) Chemical composition of the graphitic black carbon fraction in riverine and marine sediments at sub-micron scales using carbon X-ray spectromicroscopy. *Geochim Cosmochim Acta* 70(6):1483–1494.